




Solid-state reactive sintering of dense and highly conductive Ta-doped $\text{Li}_7\text{La}_3\text{Zr}_2\text{O}_{12}$ using CuO as a sintering aid

Changlong Li¹, Akihiro Ishii¹, Lindsay Roy², Dale Hitchcock², Yuqing Meng¹, and Kyle Brinkman^{1,*} 

¹Department of Materials Science and Engineering, Clemson University, Clemson, SC 29634, USA

²Savannah River National Laboratory, Aiken, SC 29808, USA

Received: 16 June 2020

Accepted: 30 August 2020

Published online:
11 September 2020

© Springer Science+Business Media, LLC, part of Springer Nature 2020

ABSTRACT

Cubic-phase garnet-type $\text{Li}_7\text{La}_3\text{Zr}_2\text{O}_{12}$ is a promising candidate for an electrolyte of all-solid-state lithium-ion batteries; however, its poor sinterability due to Li sublimation during firing has impeded large scale development. This study demonstrates a solid-state reactive sintering (SSRS) process with added CuO as a sintering aid to enable enhanced materials processing at lower temperatures. Applying the SSRS process with the addition of 1 wt% CuO decreased the sintering temperature for 0.5 mol%Ta-doped LLZTO pellets having over 90% relative density from 1250 to 1100 °C to reduce Li loss. The 1 wt% CuO addition did not lead to secondary phase formation as detected by XRD, nor to appreciable electronic conduction below 100 °C as measured by four-point probe method. The 1 wt% CuO-mixed LLZTO pellet exhibited high conductivity of approximately $3.0 \times 10^{-4} \text{ S}\cdot\text{cm}^{-1}$ (bulk) and $5.45 \times 10^{-5} \text{ S}\cdot\text{cm}^{-1}$ (grain boundary). The mechanism of CuO function as a sintering aid is presumed to be enabling liquid-phase sintering along with enhancing the decomposition of LiOH. The combined SSRS process along with optimized CuO sintering aid addition is a one-step process that is a practical technique to enhance the preparation of LLZO-based electrolyte for all-solid-state lithium-ion batteries.

Introduction

Garnet-type $\text{Li}_7\text{La}_3\text{Zr}_2\text{O}_{12}$ (LLZO) has been intensely studied as an electrolyte for all-solid-state

lithium-ion batteries because of i) its high Li^+ conductivity ($> 10^{-4} \text{ S}\cdot\text{cm}^{-1}$) [1], ii) wide electrochemical window up to 4.6 V–6.4 V [2, 3], and iii) chemical compatibility with Li metal [4]. The

Handling Editor: M. Grant Norton.

Co-authors: Changlong Li, Akihiro Ishii.

Address correspondence to E-mail: ksbrink@clemson.edu

thermodynamically most stable tetragonal phase LLZO (space group $I4_1/acd$, No. 142) has no Li vacancies and possesses relatively low Li^+ conductivity. Therefore, most investigations have focused on a cubic-phase LLZO (space group $Ia-3d$, No. 230) stabilized by donor dopants (e.g., Al^{3+} , Ga^{3+} in Li sites [5–8], Ta^{5+} in Zr sites [9, 10]) resulting in increased Li vacancies for charge compensation. However, even with the donor dopant additions, the preparation of highly conductive LLZO is still challenging because of its poor sinterability resulting from Li sublimation. Adding excess Li to green LLZO and maintaining high Li vapor pressure during sintering are general methods to suppress the Li sublimation [6, 11, 12]; however, their optimum conditions depend on a number of variables that are difficult to quantify or control. Fundamental solutions to suppress the Li sublimation are in demand to prepare dense and highly conductive cubic-phase garnet-type LLZO.

Li sublimation becomes apparent above 900 °C [13]; therefore, facilitating ion migration during sintering by the addition of sintering aids to reduce sintering duration at temperatures in excess of 900 °C is expected to improve the sinterability of LLZO. Five kinds of sintering aids that function by different mechanisms have been reported in LLZO-based materials. The sintering aid Li_3BO_3 works as non-reactive liquid medium leading liquid-phase sintering [13–16]. The remaining Li_3BO_3 does not block the Li ion conduction although its conductivity ($\approx 10^{-6}$ to 10^{-4} $\text{S}\cdot\text{cm}^{-1}$ [14, 17–19]) is lower than that of LLZO. Jonson et al. have presented that 1–2 wt% Li_3BO_3 -mixed $\text{Li}_7\text{La}_3\text{Zr}_{1.75}\text{Nb}_{0.25}\text{O}_{12}$ sintered in Ar at 1000 °C for 6 h exhibiting relatively high ionic conductivity of $2\text{--}3\times 10^{-4}$ $\text{S}\cdot\text{cm}^{-1}$ although its relative density is not reported [13]. The sintering aid Li_4SiO_4 works by accumulating impurity phases at grain boundaries during sintering [18–21]. Ta [20], Al [18], and Ta–Al-codoped [19] LLZO mixed with 5 wt% Li_4SiO_4 exhibited relative density in the range of 84–94% after sintering at 1200 °C for 24 h. A relative density of 94% and a conductivity of 3.7×10^{-4} $\text{S}\cdot\text{cm}^{-1}$ (at 33 °C) have been reported in the case of 0.6 mol % Ta-doped LLZO mixed with 1 wt% Li_4SiO_4 . The decomposition of Li_2CO_3 provides a Li_2O -rich atmosphere and the permeated Li_2O will facilitate the formation of a eutectic phase, which is also

treated as a sintering aid in some studies [22, 23]. The sintering aid MgO works by pinning grain growth. Huang et al. have reported that the growth of Ta-doped LLZO grains could be controlled to be approximately 5 μm when MgO content is higher than 4 wt% [24, 25]. 10-nm-size MgO exists at grain boundary triple junctions of the Ta-doped LLZO at the initial and intermediate stages of the sintering process, resulting in tight intergrain bonding. Zhang and Sun have recently found that CuO can be a new class of sintering aids [26]. They mixed 2 wt% CuO with a single-phase W-doped LLZO and prepared samples with 97.6% relative density by sintering at a relatively low temperature (1120 °C) for short duration (6 h). The proposed mechanism of the CuO sintering aid is that CuO (melting point 1326 °C) becomes a liquid phase during sintering and fills the grain boundary.

Among the five kinds of the sintering aids that are described in the brief review above, the effect of CuO on the sintering of LLZO may be considered the most promising. The working mechanism proposed by Zhang and Sun is different from the case of sintering other electrolyte materials (e.g., perovskite-type $\text{BaZrO}_3\text{--BaCeO}_3$ solid solution) in ceramic fuel cells [27–29]. In the case of LLZO, CuO exists in an amorphous state at the grain boundary and enables liquid-phase sintering. This is in contrast to the case of the $\text{BaZrO}_3\text{--BaCeO}_3$ solid solution where CuO is soluble in the perovskite lattice [30]. The difference may be due to reactions that occur during the sintering process: i) a conventional multistep (calcination and sintering) firing as compared to ii) a one-step solid-state reactive sintering (SSRS) process. The present work focuses on mechanism and impact of CuO sintering aids in the preparation of LLZO via the SSRS process. 0.5 mol % Ta-doped LLZO ($\text{Li}_{5.5}\text{La}_3\text{Zr}_{1.5}\text{Ta}_{0.5}\text{O}_{12}$) was used in this study as a model system because Ta can stabilize the cubic phase without blocking Li conduction paths as opposed to Al and Ga dopants [8, 31]. In this paper, the sintering behavior of the SSRS-derived Ta-doped LLZO mixed with various amount of CuO is investigated and a potential working mechanism of the CuO sintering aid in the SSRS process is proposed. An optimum CuO content in terms of electrochemical properties including ionic conductivity, electrical conductivity, and open circuit cycling is reported.

Materials and methods

0, 1, and 5 wt% CuO-mixed LLZTO were synthesized by the SSRS method using the following raw materials: LiOH (98%, Sigma-Aldrich[®]), La₂O₃ (99.99%, Acros Organics[®]), ZrO₂ (99%, Sigma-Aldrich[®]), Ta₂O₅ (99.99%, Inframat[®]), CuO (99.9%, Sigma-Aldrich[®]). The weight percent of CuO is given with respect to the total weight of the green LLZTO powder and CuO. These raw materials (20 g in total) were ball milled with 100 mL acetone (99% purity, Xtractor-Depot[®]) and 12.5 mm and 6 mm zirconia balls for 48 h in a 300 mL high-density polyethylene bottle, and then, they were dried using an infrared light for approximately 10 h. Green CuO-mixed LLZTO pellets with a dimension of 15 mm diameter and 1 mm thickness were prepared by dry pressing the dried powder at 400 MPa for 2 min. These pellets were then sintered at 1050 °C, 1100 °C, 1150 °C, and 1200 °C for 10–30 h with a heating/cooling ramp of 5 °C·min⁻¹. For reference, the LLZTO pellets were also prepared via conventional sintering technique: three-time calcination at 950 °C for 5 h followed by sintering at 1100 °C for 5 h.

The crystalline phases present, density, morphology, and electrochemical properties were investigated for the CuO-mixed LLZTO. The crystalline structure was analyzed by X-ray diffractometry (XRD, Rigaku[®] Ultima IV diffractometer) and Raman (HORIBA[®] LabRAM HR Evaluation). XRD was conducted in the two-theta range of 10 to 70 degrees with a step size of 0.1 degree. The density was measured by the Archimedes' method using the 99% pure acetone. The morphology was studied using a cold field emission scanning electron microscope (SEM, Hitachi[®] S4800) having energy-dispersive X-ray spectrometer (EDS). Since the energy of Cu-Kα (8.040 keV) is close to that of Ta-La (8.145 keV), a low accelerating voltage of 5 keV was applied. For the electrochemical measurement, electrochemical impedance spectroscopy (EIS) was conducted in a temperature range of 25 °C to 100 °C and a frequency range of 0.1 Hz to 5 MHz by applying 10 mV AC amplitude. Silver paste (Heraeus[®]) was pasted on the both sides of the sintered pure/CuO-mixed LLZTO pellets and heated at 700 °C for 30 min. The equivalent-circuit fitting for the impedance spectra was conducted using Z-view[®] provided by Scribner.

The conductivity, σ (S·cm⁻¹), of the pellets was calculated in accordance with Eq. (1):

$$\sigma = L/RS \quad (1)$$

where L is the thickness (cm), S is the cross-sectional area (cm²), and R (Ω) is the resistance of the pellets. An activation energy, E_a (eV), of the conduction was given by an Arrhenius-type plot in accordance with Eq. (2):

$$\sigma T = A \exp(-E_a/kT) \quad (2)$$

where T (K) is the temperature, A is a pre-exponential parameter, and k is a Boltzmann constant (8.6173×10^{-5} , eV·K⁻¹).

A four-wire DC measurement was conducted with a multimeter (Keithley[®] 2001) on the 1 wt% CuO-mixed LLZTO rectangular pellet (15 mm × 5 mm) in the temperature range from room temperature (25 °C) to 200 °C to determine its electronic conductivity, σ_e (S·cm⁻¹). This measurement was conducted after the temperature reached the target temperature and was maintained for 2 h duration with a ramping rate of 5 °C/min. The lithium ionic transference number, t_{Li^+} , of these pellets was determined by the following Eq. 3.

$$t_{Li^+} = \frac{\sigma - \sigma_e}{\sigma} \quad (3)$$

Open circuit voltage (OCV) of full cells consisting of the pure/CuO-mixed LLZTO as the electrolyte was conducted using a potentiostat galvanostat (SI 1287, Solartron[®]) and was recorded with CView[®] software. A Li foil (99.9%, MTI[®], ϕ 6 mm, 0.3 mm thick) was used as an anode and a composite of LiCoO₂ (\geq 98%, MTI[®]), carbon black conductive additive (Superior Graphite[®]), and polyvinylidene difluoride (PVDF, Sigma-Aldrich[®]) in a weight ratio of 90:5:5 was used for an cathode. For the cathode preparation, the LiCoO₂ powder and carbon black were mixed in N-methyl-2-pyrrolidone (NMP, \geq 99.5%, VWR[®]) solution and heated at 80 °C for 120 min, and then, it was mixed with the PVDF binder by a 5-mm-long magnetic stirring bar overnight. The full cell was assembled in an argon glovebox by painting the cathode slurry on the LLZTO pellets, heating using a vacuum oven at 150 °C overnight, mounting the Li foil on the other side of the pellet, and sealing them into a coin cell (CR2032, MTI[®]).

Results

The amount of the CuO must be optimized to avoid the formation of Cu-related secondary phases. Powder XRD patterns of the pure and the 0, 1, and 5 wt% CuO-mixed LLZTO pellets sintered at 1100 °C by SSRS process or by the conventional two-step (calcination and sintering) process are shown in Fig. 1. A pyrochlore-type $\text{La}_2\text{Zr}_2\text{O}_7$ phase appeared for the pure LLZTO pellets when sintered by the conventional process; however, no secondary phase was detected when fabricated by the SSRS process. This indicates that the Li sublimation can be suppressed by applying the SSRS method. The pyrochlore-type $\text{La}_2\text{Zr}_2\text{O}_7$ phase was detected in the 5 wt% CuO-mixed LLZTO after SSRS; however, this behavior was most likely due to Li consumption by the formation of $\text{Li}_3\text{Cu}_2\text{O}_4$. The formation of the $\text{Li}_3\text{Cu}_2\text{O}_4$ in 5 wt% CuO-mixed LLZO derivatives is consistent with the report by Zhang and Sun [26]. Meanwhile, the 1 wt% CuO-mixed LLZTO pellet contained no secondary phases that could be detected by XRD.

The addition of CuO combined with the SSRS method is expected to enhance the densification of LLZTO pellets. Cross-sectional SEM images of the pure and CuO-mixed LLZTO pellets sintered at 1100 °C for 20 h via the conventional multistep (calcination and sintering)/SSRS paths are shown in Fig. 2. For the pure LLZTO pellet sintered via the

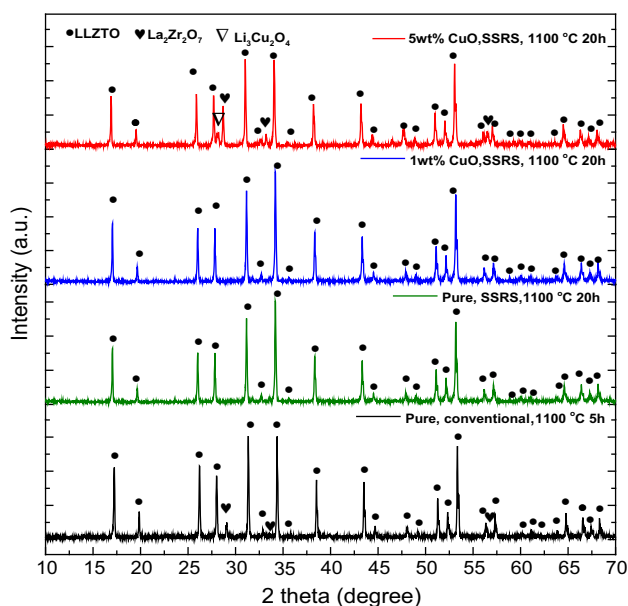


Figure 1 Powder XRD patterns of the 0, 1, and 5 wt% CuO-mixed LLZTO pellets sintered at 1100 °C.

conventional process (Fig. 2a), the grains are relatively isolated as compared to the connected grains observed in samples that were sintered via the SSRS process (Fig. 2b). The intergrain bonding was further accelerated by CuO addition, as shown in Fig. 2c and d. The morphological differences between the LLZTO mixed with 1 and 5 wt% CuO is negligible, suggesting that only the small amount (1 wt% in this case) of CuO is required to accelerate the mass-diffusion between grains. A Cu-enrichment phase was confirmed in the intergrain regions as shown in Fig. 2e.

The relative density of pure LLZTO pellets sintered via the SSRS route and the conventional multiple-step route, and that of 1 and 5 wt% CuO-mixed LLZTO pellets sintered via the SSRS route are shown in Fig. 3. The pure LLZTO pellets sintered by the SSRS process displayed higher density than those sintered by the conventional process, and the density could be further increased by CuO additions. The difference in the density between the 1 and 5 wt% CuO-mixed LLZTO was negligible, suggesting that only a small (1 wt% in this case) amount of CuO is required to enhance densification of LLZTO. Adding 1 wt% CuO combined with SSRS method, the LLZTO pellets having higher than 90% density could be prepared by sintering at 1100 °C, which temperature is 150 °C lower than the case of no CuO addition and the conventional sintering route. Comparing the relative densities of the SSRS-derived CuO-mixed LLZTO with those of the reported cubic-phase LLZO-based materials sintered with the sintering aids, the correlation relation between the relative density and the sintering-aid species is not straightforward. This implies that the densification process of these sintering-aid-mixed cubic-phase LLZO-based materials is impacted rather by other parameters (e.g., sample dimension, grain size, atmosphere, packing density of green bodies).

High Li^+ conductivity can be expected in the SSRS-derived CuO-mixed LLZTO pellets because of their high relative density in excess of 90% and their cubic crystal structure having the Li vacancies. Electrochemical impedance spectroscopy performed on a range of LLZTO materials investigated in this work: a pure LLZTO pellet sintered at 1250 °C for 5 h via the conventional multistep route; and pure, 1, and 5 wt% CuO-mixed LLZTO pellets sintered at 1100 °C for 20 h via the SSRS route. Figure 4a shows a typical impedance spectrum of the LLZTO pellets below 100 °C.

Figure 2 Cross-sectional SEM images of the LLZTO-based pellets sintered at 1100°C: **a** pure LLZTO sintered by the conventional process and **b** by the SSRS process, and, **c** 1 wt% and **d** 5 wt% CuO-mixed LLZTO pellets sintered by the SSRS process. **e** shows EDS mapping images of the 5 wt% CuO-mixed LLZTO pellet.

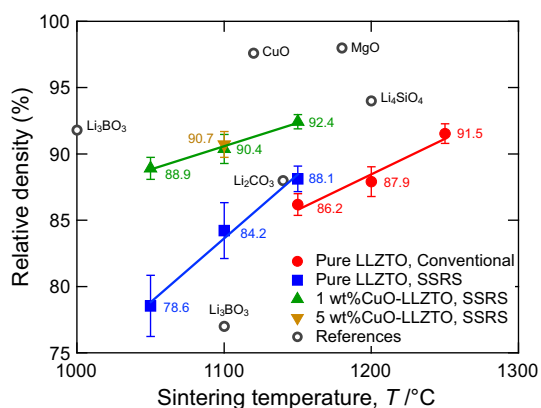
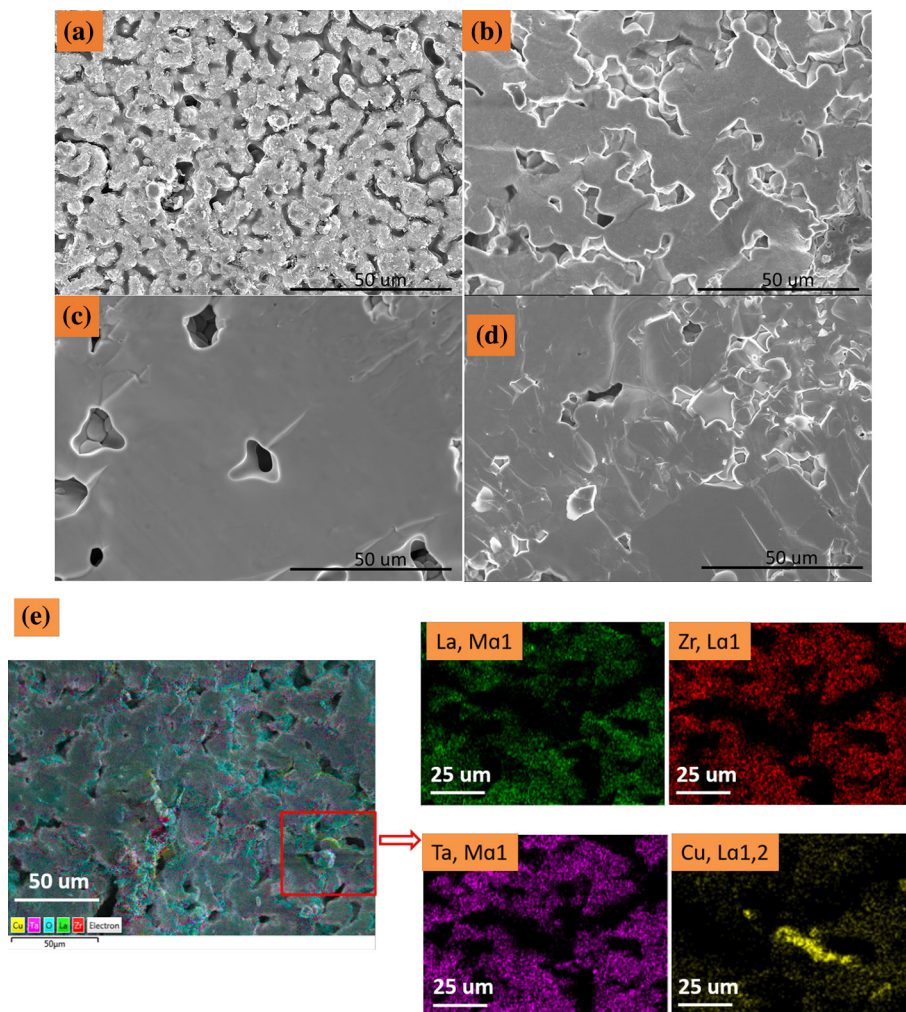


Figure 3 Relative density of the pure and CuO-mixed LLZTO pellets via the SSRS route and the conventional multiple-step route. Reference data of the cubic-phase LLZO-based materials sintered with the sintering aids [13, 15, 20, 22, 24, 26, 32] are also shown with their sintering aids.

The spectra exhibit two semicircles and a low-frequency tail. These features were fitted using one resistance attributed to bulk diffusion (R_b), two parallel circuits having a resistance and a constant phase element attributed to grain-boundary diffusion and charge transfer between LLZO and electrodes ($R_{gb} + CPE_{gb}$ and $R_{ct} + CEP_{ct}$), and one Warburg diffusion impedance (W_{diff}), as in accordance with previous reports [33–35]. At higher temperature (> 150 °C), the bulk and grain-boundary conduction could not be separated. Generally, the bulk diffusion was fit without capacitance component because of its high response to the signal. For the grain boundary diffusion and the charge transfer, the CPE component is also generally used as an alternative to the capacitance component because these processes are comprised of multiple elementary steps having different time constants. Therefore, the maximum Z'' values of these processes become less than $R/2$. Because of

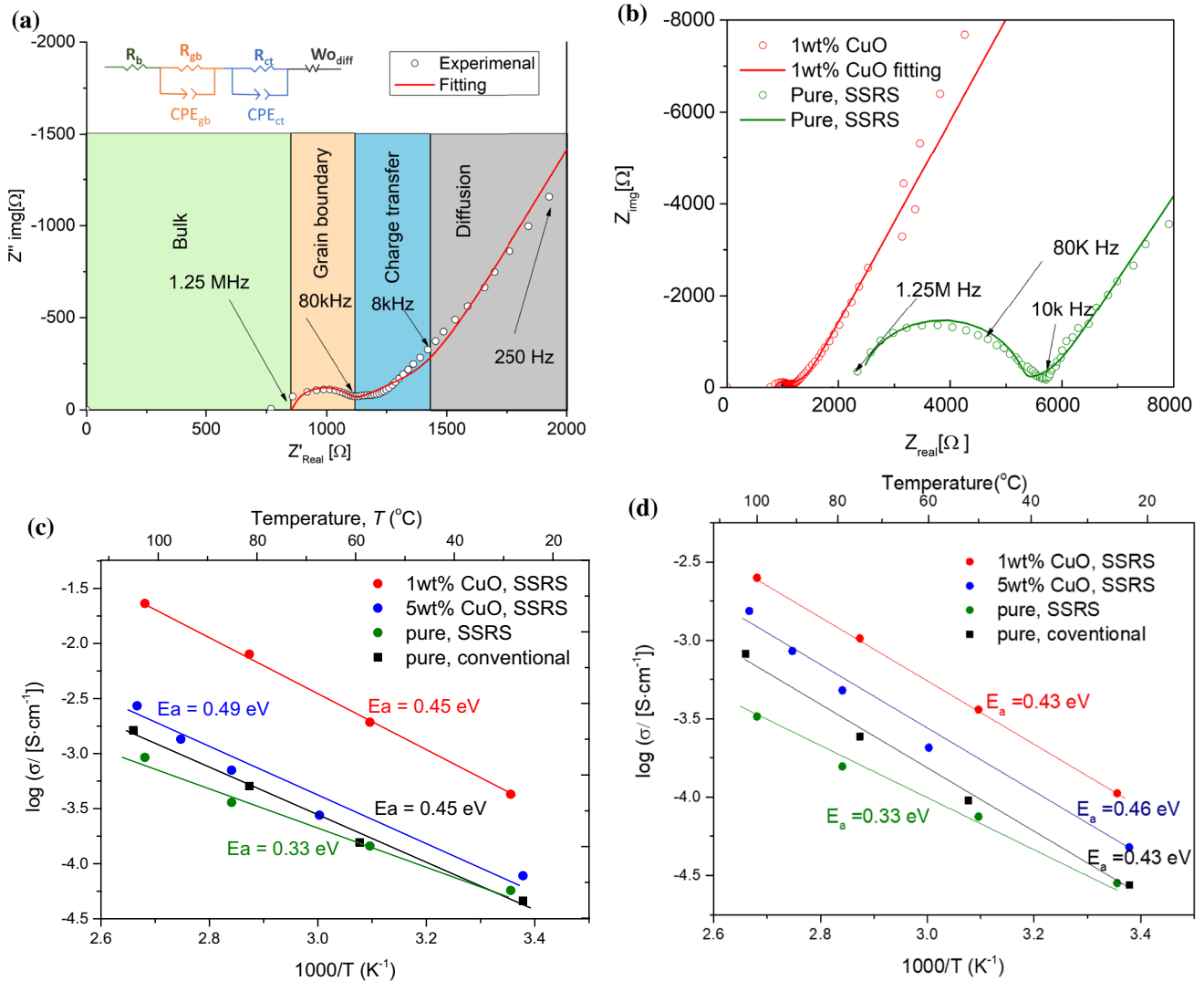


Figure 4 **a** A typical impedance spectrum of the SSRS-derived LLZTO pellets (sintering condition: SSRS 1100 °C for 20 h) and its equivalent circuit; **b** impedance spectra the SSRS-derived LLZO pellets with (1 wt% CuO) and without CuO addition

measured at 25 °C (0.15 cm thick and 1.23 cm in diameter for 1 wt% CuO, 0.19 cm thick and 1.43 cm diameter for pure sample); Arrhenius plots of **c** grain boundary and **d** total lithium-ion conductivity of the LLZTO pellets.

these multiple time constants, the existence of the two $R + CPE$ components is rarely clear; however, it is widely accepted in the field of solid-state ionics because of the physical link to the materials and necessity for fitting with small error range. The Warburg diffusion impedance represents the changing degree of oxidation/reduction reaction of the diffused ion at the electrolyte–electrode interface with decreasing frequency and theoretically provides a line with 45° slope in the Z'' - Z' Nyquist plot.

Figure 4b shows the impedance spectra of the SSRS-derived LLZTO pellets with and without CuO addition measured at room temperature. The

resistances and the related fitting parameters of each sample are listed in Table 1. The fitting errors for the resistance components and overall spectra were smaller than 5%, showing that the resistances (conductivities) given by this fitting are reliable for discussion. This table shows that the 1 wt% CuO-sample is special due to its low R_{gb} . This is consistent with the fact that the CuO aids the densification and precipitates at grain boundary; therefore, CuO does not change the bulk resistance and decreases the grain-boundary resistance. The further addition of CuO (e.g., 5 wt%) results in insignificant change in R_b but increase R_{gb} . This implies the excess CuO leads the

Table 1 Resistances and related fitting parameters of CuO-LLZTO and LLZTO samples (CS: conventional sintering)

Sample	Temperature (°C)	R_b (Ω)	R_b error (%)	R_{gb} (Ω)	R_{gb} error (%)	Overall error (%)
1wt% CuO	25	854.4	0.03	280.6	0.61	0.01
5wt% CuO	23	1222	0.41	1948	0.59	1.90
Pure, SSRS	25	2150	0.36	2089	0.29	4.17
Pure, CS	25	473.2	0.43	694.6	1.71	2.04

formation of the impurity phases (shown in Fig. 1) at the grain boundary.

Arrhenius plots of (c) the grain boundary and (d) the total conductivity for the LLZTO pellets are shown in Fig. 4. For all cases, the conductivity is higher for the bulk than for the grain boundary, and the activation energy is lower for the bulk than for the grain boundary. This is in accordance with well-known tendency among solid-state ionic conductors of that the bulk is more conductive than the grain boundary [36]. For the pure LLZTO pellets, the sintering via the conventional multistep route resulted in higher conductivity than that via the SSRS route presumably due to increased Li loss during multistep sintering which leads to the formation of the Li vacancies.

For the SSRS-derived LLZTO pellets, the addition of 1 wt% CuO resulted in the highest conductivity due to that it accelerated the densification. Compared to the addition of 1 wt% CuO, the addition of 5 wt% CuO results in lower conductivity, which is most likely because of the formation of $\text{Li}_3\text{Cu}_2\text{O}_4$ and $\text{La}_2\text{-Zr}_2\text{O}_7$ phases in the 5 wt% CuO-mixed LLZTO pellet (Fig. 1). The 1 wt% CuO-mixed LLZTO pellet indeed shows higher bulk conductivity than that of the 1 wt% CuO-mixed LLZWO pellet reported by Zhang and Sun [26]. This may be due to the contribution of either 1) Ta doping substitution on the Zr sites rather than W doping substitution on the Li sites of the LLZO, and/or 2) the use of a SSRS method as an alternative sintering method.

Table 2 presents a comparison between the SSRS-derived CuO-mixed LLZTO and reported LLZO derivatives fired with the sintering aids in terms of the sintering process, relative density, and total conductivity. The SSRS-derived CuO-mixed LLZTO shows good density of 90% and good conductivity on the order of $10^{-4} \text{ S}\cdot\text{cm}^{-1}$ even though it was made with the conventional raw ceramic powders

and fired only at once at the mild temperature of 1100 °C. This is likely due to the contribution of i) the SSRS process which reduces the total heating duration over 900 °C and therefore reduces the Li sublimation compared to the conventional sintering process, and ii) the CuO sintering aid which presumably facilitates both the phase formation and the densification. Since the SSRS process is a one-step process that can be carried out without special apparatuses and CuO is an abundant raw material, applying the SSRS process and adding CuO would be a good practical technique to prepare the LLZO-based electrolyte for the all-solid-state lithium-ion batteries.

Although the SSRS-derived 1 wt% CuO-mixed LLZTO pellet sintered at 1100 °C exhibits high levels of total conductivity, the possibility of enhancing the contribution of electronic conduction (electron/hole) by CuO addition was also studied. Four-wire DC conductivity and full-cell OCV measurements were conducted to examine a Li^+ transference number of the 1 wt% CuO-mixed LLZTO. As shown in Table 3, the 1 wt% CuO-mixed LLZTO pellet exhibited higher DC resistance than the measurement limitation ($2 \times 10^6 \Omega$) at 100 °C or below, suggesting that its DC conductivity is negligible ($< 5.70 \times 10^{-6} \text{ S}\cdot\text{cm}^{-1}$) and the Li^+ transference number is 1.00 in the temperature range. This is in agreement with the report by Zhang and Sun [26]. The pure Li^+ conduction in the 1 wt% CuO-mixed LLZTO pellet at the low temperatures is supported by that the OCV measurements of the $\text{Li}|1\text{wt}\% \text{ CuO-LLZTO}|\text{LiCoO}_2$ cell (3.78 V). The measured OCV value was larger than that of the $\text{Li}|\text{LLZTO}|\text{LiCoO}_2$ baseline cell (3.46 V), as shown in Fig. 5. These results demonstrate that CuO-mixed LLZTO is a pure lithium ionic conductor below 100 °C when the CuO concentration is limited at a low level of 1 wt%.

Table 2 Relative density and total conductivity (at 25 °C) of the cubic-phase garnet-type LLZO-based materials sintered with the sintering aids (CS: conventional sintering, BP: bed powder)

Nominal composition	Sintering aids	Methods	Temperature & duration	Relative density	Total conductivity (S·cm ⁻¹)	Activation energy (eV)	Reference
Li _{6.5} La ₃ Zr _{1.5} Ta _{0.5} O ₁₂	Li ₂ CO ₃	CS	1140 °C 16 h	88%	3.16 × 10 ⁻⁴	NA	[22]
Li ₇ La ₃ Zr ₂ O ₁₂	Li ₃ BO ₃	Sol-gel	900 °C 36 h	58%	1.9 × 10 ⁻⁵	NA	[16]
Li ₇ La ₃ Zr ₂ O ₁₂	Li ₃ BO ₃	CS	1100 °C 8 h	77%	1.61 × 10 ⁻⁵	0.58	[15]
Li ₇ La ₃ Zr _{1.75} Nb _{0.25} O ₁₂	Li ₃ BO ₃	CS	1000 °C 6 h	91.8%	1.11 × 10 ⁻⁴	NA	[13]
Li _{6.4} La ₃ Zr _{1.4} Ta _{0.6} O ₁₂	Li ₄ SiO ₄	CS	1200 °C 24 h	94%	3.21 × 10 ⁻⁴	0.38	[20]
Li _{6.4} La ₃ Zr _{1.4} Ta _{0.6} O ₁₂	None	CS	1200 °C 24 h	84%	9.24 × 10 ⁻⁵	0.43	[20]
Li _{6.4} La ₃ Zr _{1.4} Ta _{0.6} O ₁₂	MgO, BP	CS	1180 °C 5 h	98%	3.35 × 10 ⁻⁴	0.43	[24]
Li _{6.3} La ₃ Zr _{1.65} W _{0.35} O ₁₂	CuO	CS	1120 °C 6 h	97.6%	1.11 × 10 ⁻⁴	0.38	[26]
Li _{6.5} La ₃ Zr _{1.5} Ta _{0.5} O ₁₂	CuO	SSRS	1100 °C 20 h	90.38%	1.06 × 10 ⁻⁴	0.43	This work

Some of the conductivity at 25 °C and the activation energy are calculated by extrapolation of the given data

Table 3 Temperature-dependent AC/DC conductivities and transference numbers of the 1wt% CuO-mixed LLZTO pellet sintered at 1100 °C and 2 wt% CuO-mixed LLZWO reported by Zhang and Sun [26]

Materials	Temperature (°C)	AC total conductivity (S·cm ⁻¹)	DC conductivity (S·cm ⁻¹)	Li ⁺ transference numbers
1wt% CuO-mixed LLZTO (this work)	25	1.06 × 10 ⁻⁴	< 5.70 × 10 ⁻⁶	1.00
	50	3.62 × 10 ⁻⁴	< 5.70 × 10 ⁻⁶	1.00
	100	2.51 × 10 ⁻³	< 5.70 × 10 ⁻⁶	1.00
	150	1.29 × 10 ⁻²	7.47 × 10 ⁻⁵	0.994
	200	3.16 × 10 ⁻²	2.36 × 10 ⁻⁴	0.993
2 wt% CuO-mixed LLZWO (Zhang and Sun [26])	25	1.88 × 10 ⁻⁴	1.388 × 10 ⁻⁸	1.00

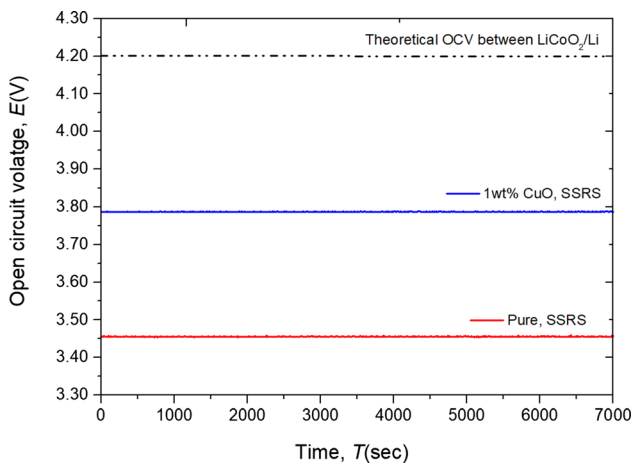


Figure 5 OCV of the Li| pure or 1wt% CuO-mixed LLZTO|LiCoO₂ cells at room temperature.

Discussion

In order to investigate the mechanism of CuO enhanced sintering of the LLZTO, the phase evolution behavior of the 1wt% CuO-LLZTO pellet was analyzed by XRD and Raman spectroscopy. The XRD patterns of the CuO-LLZTO fired at 700 °C, 800 °C, 900 °C, and 1000 °C are shown in Fig. 4a. The formation of a K₂NiF₄-type La₂Cu_{0.5}Li_{0.5}O₄ phase was confirmed at 700 °C and 800 °C, and this phase disappears at temperatures above 900 °C. This assessment of the phase evolution is consistent with the Raman spectra shown in Fig. 6b. According to Zhang et al., the Raman peaks of the cubic-phase garnet-type LLZO that appear in ranges of 200–300 and 300–450 cm⁻¹ are corresponding to bonding of Li–O₆,

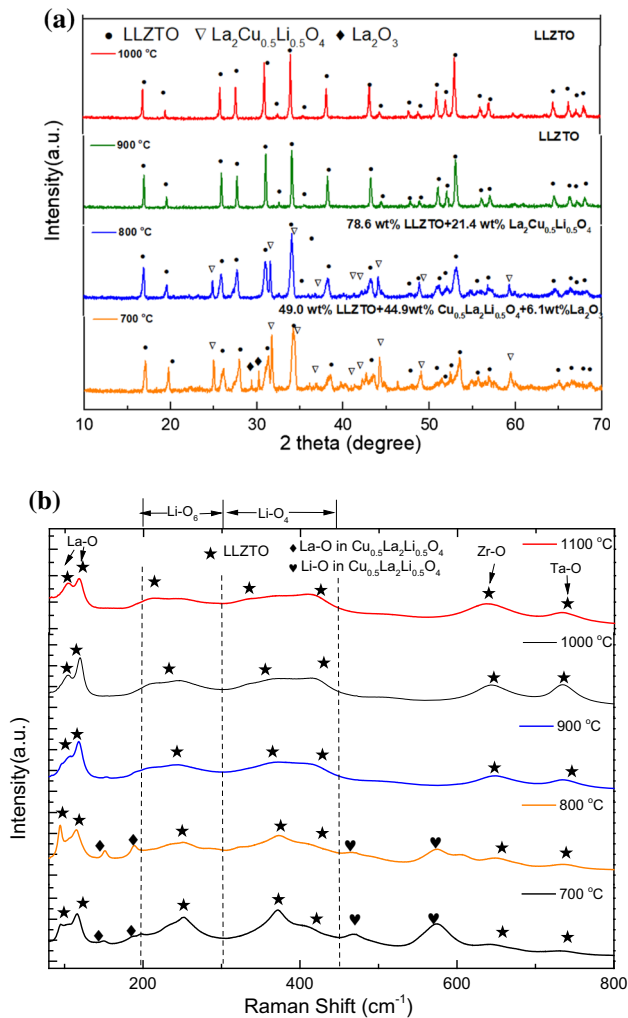


Figure 6 **a** XRD patterns and **b** Raman spectra of the 1 wt% CuO-mixed LLZTO pellets sintered at 700–1000 °C. The abundance ratios of the phases are also shown in **a**.

Li-O_4 , respectively. The detailed assignments are given in Table 4. For the 1 wt% CuO-mixed LLZTO pellet, the main Raman peaks 109.97 cm^{-1} (T_{2g}),

118.09 cm^{-1} (E_g) are attributed to vibration of La–O bonds. Peaks located at 239.38 cm^{-1} (A_{1g}), 369.02 cm^{-1} (T_{2g}), 410 cm^{-1} (T_{2g}/E_{2g}), 634.87 cm^{-1} (A_{1g}), 731.16 cm^{-1} belong to Li–O vibration. The Raman peaks at 634.87 cm^{-1} and 737.16 cm^{-1} are attributed to vibrations of $^1\text{Zr-O}$ and Ta–O, respectively. All the peaks match with the reported peaks of the cubic-phase garnet-type LLZO [37, 38]. In addition to these peaks, at 700 °C and 800 °C, extra Raman peaks at 151.342 cm^{-1} , 188.552 cm^{-1} , 575.241 cm^{-1} , and 606.6 cm^{-1} were confirmed. These peaks are attributed to vibration of La–O and Li–O in the $\text{La}_2\text{Cu}_{0.5}\text{Li}_{0.5}\text{O}_4$ phase. This XRD-Raman analysis suggests that the intermediate $\text{La}_2\text{Cu}_{0.5}\text{Li}_{0.5}\text{O}_4$ phase may play an important role in the sintering process of LLZTO.

Taking these results into consideration, the potential sintering mechanism of the CuO-mixed LLZTO via the SSRS route can be proposed as shown in Fig. 7. Although LiOH does not turn to Li_2O oxide up to 1000 °C [41], LiOH in the green LLZTO mixture can become the crystalline oxide as the LLZTO at lower temperature (680 °C [42]) by the virtue of the Gibbs free energy for the formation of the garnet-type LLZTO phase (ΔG_{garnet}). This determines the relative position of the black, blue, and green lines in Fig. 7. The oxidation temperature is further reduced by the addition of CuO in the system owing to the formation energy of the K_2NiF_4 -type $\text{La}_2\text{Cu}_{0.5}\text{Li}_{0.5}\text{O}_4$ phase ($\Delta G_{\text{K}_2\text{NiF}_4}$). The preferential formation of the $\text{La}_2\text{Cu}_{0.5}\text{Li}_{0.5}\text{O}_4$ phase in the early stage of the sintering can be seen in Fig. 6a. This determines the relative position of the black, green, and red lines in Fig. 7. This denotes that the temperature for the formation of LLZTO is reduced by the addition of CuO. At 900 °C, the $\text{La}_2\text{Cu}_{0.5}\text{Li}_{0.5}\text{O}_4$ phase decomposed resulting in La^{3+} and Li^+ incorporation into LLZTO,

Table 4 Raman peak position, vibrational mode assignment, their references, and bonding mode for the LLZO-based materials

Peak positions (cm^{-1})	Vibrational modes	References (Kumar et al. [37] & Rupp et al. [39])	Bonding mode (Zhang et al. [40])
110	T_{2g}	107	La–O
118	E_g	121	La–O
240	A_{1g}	340	Li– O_6
369	T_{2g}	361	Li– O_4
410	T_{2g}/E_{2g}	410	
	T_{2g}/E_g	514	
635	A_{1g}		Zr–O
731			Ta–O

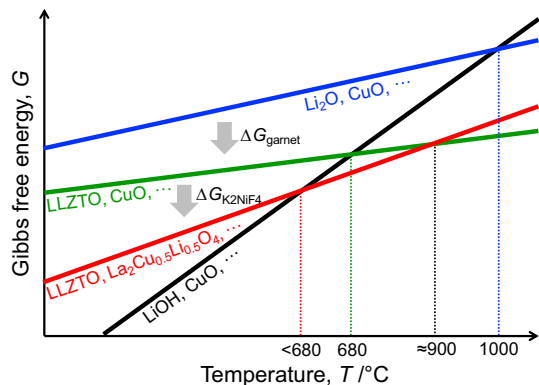


Figure 7 Estimated relation of the Gibbs free energies for the CuO-mixed LLZTO system.

whereas Cu^{2+} most likely forms molten CuO. Although the melting point of CuO is 1326 °C, it can be molten even at this temperature range when it exists with Li^+ [43]. Although no direct evidence of molten CuO was obtained in this material system by using transmission electron microscopy, Zhang and Sun have confirmed that molten CuO exists at the grain boundary in the case of a similar system, W-doped LLZO [26]. The CuO-based melt fills the grain boundary and accelerates the ion migration of the sintering process [26]. It is thought that CuO works as a sintering aid by the promotion of phase formation of crystalline and the ion migration. Additional details of these processes may be studied in depth in future work by analyzing thermodynamic parameters of the LLZTO and $\text{La}_2\text{Cu}_{0.5}\text{Li}_{0.5}\text{O}_4$ phases using techniques such as high temperature melt solution calorimetry [44, 45].

Conclusion

This study showed that the SSRS process and adding CuO are beneficial to prepare dense LLZTO electrolytes. Applying the SSRS process and adding 1 wt% CuO could be lowered the sintering temperature for the LLZTO pellets having over 90% density from 1250 to 1100 °C. Whereas 5 wt% CuO addition resulted in the evolution of the Cu-related secondary phase, 1 wt% CuO addition resulted in no secondary phases at the XRD level and no electronic conduction below 100 °C. The 1 wt% CuO-mixed LLZTO pellet exhibited the good conductivity of $\sim 2.99 \times 10^{-4} \text{ S}\cdot\text{cm}^{-1}$ (bulk) and $\sim 4.44 \times 10^{-5} \text{ S}\cdot\text{cm}^{-1}$ (grain boundary) at room temperature (25 °C). In addition,

the overall conductivity of 1wt% CuO also reached to $\sim 10^{-4} \text{ S}\cdot\text{cm}^{-1}$ level, which was comparable with related work. Judging from the formation of the K_2NiF_4 -type $\text{La}_2\text{Cu}_{0.5}\text{Li}_{0.5}\text{O}_4$ intermediate phase in the heating-up process, CuO works as the sintering aid presumably not only by enabling liquid-phase sintering but also by promoting the decomposition of LiOH. The combined SSRS process along with optimized CuO sintering aid addition is a one-step process that is a practical technique to enhance the preparation of LLZO-based electrolyte for all-solid-state lithium-ion batteries.

Acknowledgement

KSB acknowledges support of SRNL LDRD through SRNS TASK ORDER AGREEMENT (TOA) 0000453661 “Solid State Ionics: Advanced Manufacturing.”

References

- [1] Murugan R, Thangadurai V, Weppner W (2007) Fast lithium ion conduction in garnet-type $\text{Li}_7\text{La}_3\text{Zr}_2\text{O}_{12}$. *Angew Chem Int Ed* 46:7778–7781. <https://doi.org/10.1002/anie.200701144>
- [2] Liu M, Li X, Wang X et al (2018) Facile synthesis and electrochemical properties of high lithium ionic conductivity $\text{Li}_{1.7}\text{Al}_{1.0}\text{Ti}_{1.7}\text{Si}_{0.4}\text{P}_{2.6}\text{O}_{12}$ ceramic solid electrolyte. *J Alloys Comp* 756:103–110. <https://doi.org/10.1016/j.jallcom.2018.04.333>
- [3] Thompson T, Yu S, Williams L et al (2017) Electrochemical window of the Li-Ion Solid Electrolyte $\text{Li}_7\text{La}_3\text{Zr}_2\text{O}_{12}$. *ACS Energy Lett* 2:462–468. <https://doi.org/10.1021/acsenergylett.6b00593>
- [4] Han F, Zhu Y, He X et al (2016) Electrochemical stability of $\text{Li}_{10}\text{GeP}_2\text{S}_{12}$ and $\text{Li}_7\text{La}_3\text{Zr}_2\text{O}_{12}$ solid electrolytes. *Adv Energy Mater* 6:1–9. <https://doi.org/10.1002/aenm.201501590>
- [5] Rettenwander D, Blaha P, Laskowski R et al (2014) DFT study of the role of Al^{3+} in the fast ion-conductor $\text{Li}_{7-3x}\text{Al}_3\text{La}_3\text{Zr}_2\text{O}_{12}$ garnet. *Chem Mater* 26:2617–2623. <https://doi.org/10.1021/cm5000999>
- [6] Wagner R, Redhammer GJ, Rettenwander D et al (2016) Crystal structure of garnet-related Li-Ion conductor $\text{Li}_{7-3x}\text{GaxLa}_3\text{Zr}_2\text{O}_{12}$: fast Li-Ion conduction caused by a different cubic modification? *Chem Mater* 28:1861–1871. <https://doi.org/10.1021/acs.chemmater.6b00038>

- [7] Robben L, Merzlyakova E, Heitjans P, Gesing TM (2016) Symmetry reduction due to gallium substitution in the garnet $\text{Li}_{6.43(2)}\text{Ga}_{0.52(3)}\text{La}_{2.67(4)}\text{Zr}_2\text{O}_{12}$. *Acta Cryst Sect E Cryst Commun* 72:287–289. <https://doi.org/10.1107/S2056989016001924>
- [8] Rettenwander D, Langer J, Schmidt W et al (2015) Site Occupation of Ga and Al in Stabilized Cubic $\text{Li}_{7-3(x+y)}\text{Ga}_x\text{Al}_y\text{La}_3\text{Zr}_2\text{O}_{12}$ Garnets As Deduced from ^{27}Al and ^{71}Ga MAS NMR at Ultrahigh Magnetic Fields. *Chem Mater* 27:3135–3142. <https://doi.org/10.1021/acs.chemmater.5b00684>
- [9] Gu W, Ezbi M, Prasada Rao R et al (2015) Effects of pentavalent and trivalent dopants on structure and conductivity of $\text{Li}_7\text{La}_3\text{Zr}_2\text{O}_{12}$. *Solid State Ion* 274:100–105. <https://doi.org/10.1016/j.ssi.2015.03.019>
- [10] Thompson T, Wolfenstine J, Allen JL et al (2014) Tetragonal vs. cubic phase stability in Al-free Ta doped $\text{Li}_7\text{La}_3\text{Zr}_2\text{O}_{12}$ (LLZO). *J Mater Chem A* 2:13431–13436. <https://doi.org/10.1039/c4ta02099e>
- [11] Rettenwander D, Redhammer G, Preishuber-Pflügl F et al (2016) Structural and electrochemical consequences of Al and Ga Cosubstitution in $\text{Li}_7\text{La}_3\text{Zr}_2\text{O}_{12}$ solid electrolytes. *Chem Mater* 28:2384–2392. <https://doi.org/10.1021/acs.chemmater.6b00579>
- [12] Hubaud AA, Schroeder DJ, Ingram BJ et al (2015) Thermal expansion in the garnet-type solid electrolyte ($\text{Li}_7 - \text{Al}/3$) $\text{La}_3\text{Zr}_2\text{O}_{12}$ as a function of Al content. *J Alloys Comp* 644:804–807. <https://doi.org/10.1016/j.jallcom.2015.05.067>
- [13] Jonson RA, McGinn PJ (2018) Tape casting and sintering of $\text{Li}_7\text{La}_3\text{Zr}_1.75\text{Nb}_0.25\text{Al}_0.1\text{O}_{12}$ with Li_3BO_3 additions. *Solid State Ion* 323:49–55. <https://doi.org/10.1016/j.ssi.2018.05.015>
- [14] Shin RH, Son SI, Lee SM et al (2016) Effect of Li_3BO_3 additive on densification and ion conductivity of garnet-type $\text{Li}_7\text{La}_3\text{Zr}_2\text{O}_{12}$ solid electrolytes of all-solid-state lithium-ion batteries. *J Korean Ceram Soc* 53:712–718. <https://doi.org/10.4191/kcers.2016.53.6.712>
- [15] Ohta S, Komagata S, Seki J et al (2013) All-solid-state lithium ion battery using garnet-type oxide and Li_3BO_3 solid electrolytes fabricated by screen-printing. *J Power Sources* 238:53–56. <https://doi.org/10.1016/j.jpowsour.2013.02.073>
- [16] Tadanaga K, Takano R, Ichinose T et al (2013) Low temperature synthesis of highly ion conductive $\text{Li}_7\text{La}_3\text{Zr}_2\text{O}_{12}$ - Li_3BO_3 composites. *Electrochem Commun* 33:51–54. <https://doi.org/10.1016/j.elecom.2013.04.004>
- [17] Takano R, Tadanaga K, Hayashi A, Tatsumisago M (2014) Low temperature synthesis of Al-doped $\text{Li}_7\text{La}_3\text{Zr}_2\text{O}_{12}$ solid electrolyte by a sol-gel process. *Solid State Ion* 255:104–107. <https://doi.org/10.1016/j.ssi.2013.12.006>
- [18] Janani N, Deviannapoorani C, Dhivya L, Murugan R (2014) Influence of sintering additives on densification and Li + conductivity of Al doped $\text{Li}_7\text{La}_3\text{Zr}_2\text{O}_{12}$ lithium garnet. *RSC Adv* 4:51228–51238. <https://doi.org/10.1039/c4ra08674k>
- [19] Wakudkar P, Deshpande AV (2019) Effect of Li_4SiO_4 addition in $\text{Li}_{6.22}\text{Al}_{0.16}\text{La}_3\text{Zr}_{1.7}\text{Ta}_{0.3}\text{O}_{12}$ garnet type solid electrolyte for lithium ion battery application. *Ceram Int* 45:20113–20120. <https://doi.org/10.1016/j.ceramint.2019.06.276>
- [20] Janani N, Ramakumar S, Kannan S, Murugan R (2015) Optimization of lithium content and sintering aid for maximized Li + conductivity and density in Ta-Doped $\text{Li}_7\text{La}_3\text{Zr}_2\text{O}_{12}$. *J Am Ceram Soc* 98:2039–2046. <https://doi.org/10.1111/jace.13578>
- [21] Deng Y, Eames C, Fleutot B et al (2017) Enhancing the Lithium Ion Conductivity in Lithium Superionic Conductor (LISICON) solid electrolytes through a mixed polyanion effect. *ACS Appl Mater Interfaces* 9:7050–7058. <https://doi.org/10.1021/acsami.6b14402>
- [22] Liu K, Ma JT, Wang CA (2014) Excess lithium salt functions more than compensating for lithium loss when synthesizing $\text{Li}_{6.5}\text{La}_3\text{Ta}_{0.5}\text{Zr}_{1.5}\text{O}_{12}$ in alumina crucible. *J Power Sources* 260:109–114. <https://doi.org/10.1016/j.jpowsour.2014.02.065>
- [23] Huang Z, Liu K, Chen L et al (2017) Sintering behavior of garnet-type $\text{Li}_{6.4}\text{La}_3\text{Zr}_{1.4}\text{Ta}_{0.6}\text{O}_{12}$ in Li_2CO_3 atmosphere and its electrochemical property. *Int J Appl Ceram Technol* 14:921–927. <https://doi.org/10.1111/ijac.12735>
- [24] Huang X, Xiu T, Badding ME, Wen Z (2018) Two-step sintering strategy to prepare dense Li-Garnet electrolyte ceramics with high Li + conductivity. *Ceram Int* 44:5660–5667. <https://doi.org/10.1016/j.ceramint.2017.12.217>
- [25] Huang X, Lu Y, Song Z et al (2019) Preparation of dense Ta-LLZO/MgO composite Li-ion solid electrolyte: sintering, microstructure, performance and the role of MgO. *J Energy Chem* 39:8–16. <https://doi.org/10.1016/j.jechem.2019.01.013>
- [26] Zhang W, Sun C (2019) Effects of CuO on the microstructure and electrochemical properties of garnet-type solid electrolyte. *J Phys Chem Solids* 135:109080. <https://doi.org/10.1016/j.jpcs.2019.109080>
- [27] Ueno K, Hatada N, Han D, Uda T (2019) Thermodynamic maximum of γ doping level in barium zirconate in co-sintering with NiO. *J Mater Chem A* 7:7232–7241. <https://doi.org/10.1039/c8ta12245h>
- [28] Wang B, Bi L, Zhao XS (2018) Exploring the role of NiO as a sintering aid in $\text{BaZr}_{0.1}\text{Ce}_{0.7}\text{Y}_{0.2}\text{O}_{3-\delta}$ electrolyte for proton-conducting solid oxide fuel cells. *J Power Sources*

- 399:207–214. <https://doi.org/10.1016/J.JPOWSOUR.2018.07.087>
- [29] Tong J, Clark D, Bernau L et al (2010) Solid-state reactive sintering mechanism for large-grained yttrium-doped barium zirconate proton conducting ceramics. *J Mater Chem* 20:6333–6341. <https://doi.org/10.1039/c0jm00381f>
- [30] Nikodemski S, Tong J, O'Hayre R (2013) Solid-state reactive sintering mechanism for proton conducting ceramics. *Solid State Ion* 253:201–210. <https://doi.org/10.1016/j.ssi.2013.09.025>
- [31] Chen F, Li J, Huang Z et al (2018) Origin of the Phase Transition in Lithium Garnets. *J Phys Chem C* 122:1963–1972. <https://doi.org/10.1021/acs.jpcc.7b10911>
- [32] Krevit L (1988) Database Management Systems. *Med Ref Serv Q* 6:65–68. https://doi.org/10.1300/J115v06n04_07
- [33] Wu J-F, Chen E-Y, Yu Y et al (2017) Gallium-Doped Li₇La₃Zr₂O₁₂ garnet-type electrolytes with high lithium-ion conductivity. *ACS Appl Mater Interfaces* 9:1542–1552. <https://doi.org/10.1021/acsami.6b13902>
- [34] Zhu Y, Connell JG, Tepavcevic S et al (2019) Dopant-Dependent Stability of Garnet Solid Electrolyte Interfaces with Lithium Metal. *Adv Energy Mater*. 9:1803440–1803451. <https://doi.org/10.1002/aenm.201803440>
- [35] Chen X, Wang T, Lu W et al (2018) Synthesis of Ta and Ca doped Li₇La₃Zr₂O₁₂ solid-state electrolyte via simple solution method and its application in suppressing shuttle effect of Li-S battery. *J Alloys Comp* 744:386–394. <https://doi.org/10.1016/j.jallcom.2018.02.134>
- [36] Li C, Liu Y, He J, Brinkman KS (2017) Ga-substituted Li₇La₃Zr₂O₁₂: an investigation based on grain coarsening in garnet-type lithium ion conductors. *J Alloys Comp* 695:3744–3752. <https://doi.org/10.1016/j.jallcom.2016.11.277>
- [37] Kumar PJ, Nishimura K, Senna M et al (2016) A novel low-temperature solid-state route for nanostructured cubic garnet Li₇La₃Zr₂O₁₂ and its application to Li-ion battery. *RSC Adv* 6:62656–62667. <https://doi.org/10.1039/c6ra09695f>
- [38] Elisabeth M, Reyer A, Rettenwander D, et al A Raman spectroscopic study on fast ionic conducting variants of Li₇La₃Zr₂O₁₂. In Conference XXV ICORS2016
- [39] Pfenninger R, Struzik M, Garbayo I et al (2019) A low ride on processing temperature for fast lithium conduction in garnet solid-state battery films. *Nat Energy*. 4:475–483. <https://doi.org/10.1038/s41560-019-0384-4>
- [40] Zhang Y, Deng J, Hu D et al (2019) Synergistic regulation of garnet-type Ta-doped Li₇La₃Zr₂O₁₂ solid electrolyte by Li + concentration and Li + transport channel size. *Electrochim Acta*. 296:823–829. <https://doi.org/10.1016/j.electacta.2018.11.136>
- [41] Beyer H, Meini S, Tsiouvaras N et al (2013) Thermal and electrochemical decomposition of lithium peroxide in non-catalyzed carbon cathodes for Li-air batteries. *Phys Chem Chem Phys* 15:11025–11037. <https://doi.org/10.1039/c3cp51056e>
- [42] Geng H, Chen K, Yi D et al (2016) Formation mechanism of garnet-like Li₇La₃Zr₂O₁₂ powder prepared by solid state reaction. *Rare Metal Mater Eng* 45:612–616. [https://doi.org/10.1016/s1875-5372\(16\)30081-9](https://doi.org/10.1016/s1875-5372(16)30081-9)
- [43] Abdullaev GK, Mamedov KhS, Buludov NT (1982) Sodium oxide-cadmium oxide-boron oxide system. *Zh Neorg Khim* 27(11):2948
- [44] Zhao M, Russell P, Amoroso J et al (2020) Exploring the links between crystal chemistry, cesium retention, thermochemistry and chemical durability in single-phase andite. *J Mater Sci*. 55:6401–6416. <https://doi.org/10.1007/s10853-020-04447-3>
- [45] Grote R, Zhao M, Shuller-Nickles L et al (2019) Compositional control of tunnel features in hollandite-based ceramics: structure and stability of (Ba,Cs)_{1.33}(Zn,Ti)₈O₁₆. *J Mater Sci*. 54:1112–1125. <https://doi.org/10.1007/s10853-018-2904-1>

Publisher's Note Springer Nature remains neutral with regard to jurisdictional claims in published maps and institutional affiliations.